Journal of
Materials Chemistry A
Materials for energy and sustainability

This article can be cited before page numbers have been issued, to do this please use: J. Tao, C. Zhang, X. Li, X. Chen, C. Ji, W. Wan and C. Wang, *J. Mater. Chem. A*, 2024, DOI: 10.1039/D4TA02431A.

ROYAL SOCIETY OF CHEMISTRY

rsc.li/materials-a

Journal of Materials Chemistry A

View Article Online
DOI: 10.1039/D4TA02431A

PAPER

Advancing Anode-Less Lithium Metal Batteries: ZnF$_2$ Modification and In-Situ Structural Regulation for Enhanced Performance

Jing Tao,[a] Can Zhang,[a] Xueyang Li,[a] Xinlong Chen,[a] Chenzhen Ji[b], Wang Wan*[a] and Chao Wang*[a]

Received 00th January 20xx,
Accepted 00th January 20xx

DOI: 10.1039/x0xx00000x

Lithium metal anode tends to form non-uniform Li deposition and cause dendrite growth during cycling. Meanwhile, the deposition and dissolution of lithium metal often result in the continuous formation and breakdown of the SEI. Additionally, the use of thick lithium metal often results in an excessive inventory of lithium, which diminishes the energy advantage of lithium metal. It is challenging to fabricate thin lithium foils due to its low mechanical strength. To address these issues, we employ an in-situ structural regulation strategy to prepare high-performance lithium metal batteries. In this paper, the mechanical strength of the LiF@LiZn10/Li foil is significantly enhanced, allowing it to be thinned down to a thickness of 5 µm, accompanied by great air stability. The in-situ formation of LiZn alloys improves the Li deposition behavior. Furthermore, we have demonstrated the participation of LiF particles in the in-situ formation of the SEI, which facilitates Li$^+$ transport kinetics. The LiF@LiZn10/Li electrode demonstrates significantly enhanced cycling performance by synergistically improving Li deposition behavior and optimizing the SEI layer in situ. The LiF@LiZn10/Li foil electrode exhibits a long cycle life of over 1300 hours at 1 mA cm^{-2} and 1 mA h cm^{-2}. When coupled with a commercial LiFePO$_4$ cathode (3.3 mA h cm^{-2}), LiFePO$_4$||LiF@LiZn10/Li cell exhibited approximately triple the cycling life compared to cells with LMBs. This work provides a novel strategy to optimize LMAs for next-generation LMBs.

Introduction

The increasing demand for high-energy-density batteries has revitalized interest in lithium metal anodes (LMAs). Possessing an ultrahigh theoretical specific capacity of 3860 mA h g^{-1}, low density of 0.59 g cm^{-3} and the most negative electrochemical potential (-3.04 V vs. the SHE), lithium metal emerges as an attractive solution for advanced battery technologies.[1, 2] However, the practical application of lithium metal anodes faces several challenges. Unlike the graphite anode based on the Li$^+$ insertion mechanism, lithium metal anode can achieve a direct Li deposition and lithium dissolution process.[3, 4] This process encounters numerous challenges, including the uncontrollable growth of lithium dendrites, significant volume change,[5] and the continuous formation of solid electrolyte interphase (SEI) layers.[6, 7] These issues can lead to various complications, such as short circuits, the formation of dead lithium, pulverization, and low Coulombic efficiency.[8, 9] Consequently, these factors result in irreversible capacity loss and decreased cycle life, and in severe cases, they can even cause safety issues such as fires and explosions.[10, 11] Overall, these challenges severely hinder the development of lithium-metal batteries.

The behavior of Li deposition is largely influenced by lithium nucleation and Li$^+$ transport within lithium anode materials.[12] Lithium dendrite formation and growth primarily result from random Li$^+$ nucleation sites and uneven distribution of local current density.[13] To address this challenge, establishing uniform nucleation sites using lithiophilic materials can promote uniform nucleation and facilitate homogeneous Li deposition, thereby significantly reducing the nucleation overpotential of the lithium electrode.[14, 15]

Introducing appropriate Li-metal alloys with good lithium affinity and wetting properties can effectively provide uniform and abundant deposition sites, preventing the growth of dendrites during electrochemical cycling processes. Zn as a material with good lithium affinity and wetting properties can effectively provide uniform and abundant deposition sites, preventing the growth of dendrites during electrochemical cycling processes.[16-19] The uniform dispersion of nanoscale LiAl alloys within the matrix is beneficial for inducing the uniform deposition of metallic lithium and effectively suppressing side reactions.[20] LiSn alloys also have a lower nucleation barrier for lithium and exhibit great lithiophilicity, which can regulate the deposition and stripping behavior of Li$^+$.[15, 21] The direct incorporation of alloying elements into molten lithium facilitates the formation of in-situ Li-M alloys frameworks,[22] serving as mixed ions and electron conductors (MIECs).[23, 24]

The inherent reactivity and significant volume changes observed during the cycling of lithium metal often result in the continuous formation and breakdown of the SEI, leading to the consumption of active lithium materials and electrolytes.[25] This phenomenon not only contributes to a notable reduction in Coulombic efficiency but also leads to electrode pulverization.[26, 27] To address these challenges, researchers have explored methods to enhance the stability and mechanical integrity of the SEI layer. Incorporating lithium fluoride (LiF) into the SEI has been shown to improve its chemical stability and mechanical strength, thereby facilitating a stable interface between LMAs and corrosive solvent molecules.[28]

---

[a] School of Materials Science and Engineering, Tongji University, Shanghai 201804, China. E-mail: chaow@tongji.edu.cn
[b] School of Mechanical Engineering, Tongji University, Jiading District, Shanghai 201804, China.

†Electronic Supplementary Information (ESI) available. See DOI: 10.1039/x0xx00000

View Article Online
DOI: 10.1039/D4TA02461A

Optimizing the formation of a LiF-rich SEI can be achieved through the utilization of fluorinated solvents, additives, and negative electrodes containing fluorine.[29, 30]

Furthermore, many lithium metal batteries (LMBs) investigated in previous studies utilize thick lithium foil exceeding 300 μm as the anode, leading to a significant excess of lithium that diminishes the energy advantage of using lithium metal as the anode. For instance, employing a 300 μm-thick lithium metal anode (equivalent to an areal capacity of 60 mA h cm^{-2}) alongside a commercial cathode with a capacity of 3 mA h cm^{-2}, the energy density achieved by using lithium as the anode is lower than that obtained with graphite, and with considerably poorer cycling stability.[31] Taking a pragmatic approach, it is evident that only the utilization of thin lithium metal anodes, typically less than 50 μm, can yield advantages for high-energy-density batteries.[32]

However, it is challenging to fabricate thin lithium foils due to the low mechanical strength of lithium metal.[33] To address this limitation, researchers have begun to explore lithium alloys to enhance the machinability of lithium metal for preparing ultrathin lithium foils. By incorporating silver into lithium metal to form LiAg alloys, the machinability of lithium metal can be greatly improved, enabling the fabrication of ultrathin lithium foils. [34, 35] By utilizing the lithiophilicity of LiZn alloys, the molten LiZn alloys can easily spread on a copper foil and form a controllable thickness negative electrode.[18] Additionally, LiSn alloys enable the large-scale printing of flexible ultrathin (15 μm) lithium alloy negative electrodes.[36]

When designing and optimizing LMAs, one of the primary considerations is the use of lithiophilic elements. Among lithiophilic materials, lithium alloying materials have garnered significant attention, which not only enhances the mechanical properties but also improves the deposition behavior of lithium. Here, we evaluated a range of alloying materials based on their lithiophilic degree, cost, deposition behavior, volume stability, and other factors to identify suitable materials. Furthermore, the formation of a LiF-rich SEI has been found to be highly beneficial for LMAs.[37] Taking inspiration from this, our experiments further introduced LiF particles, which contribute to the formation of an SEI rich in LiF based on introducing lithiophilic elements. In this study, we introduced metal fluorides (MF_n) into lithium. Metal fluorides react with molten lithium to produce LiF particles and LiM alloys, typically n >= 2. The reactions are demonstrated as follows:

$$\mathrm{Li} + \mathrm{MF}_n \rightarrow n\,\mathrm{LiF} + \mathrm{Li} \tag{1}$$

$$\mathrm{Li} + \mathrm{M} \rightarrow \mathrm{LiM} \tag{2}$$

By doing so, we can create a uniform Li-alloy foil with enhanced mechanical strength, facilitating the fabrication of thin Li-alloy foils. The introduction of the alloy modulates Li deposition behavior, and a LiF-rich foil can gradually release LiF, thereby in-situ regulating SEI during cycling. It effectively improves the electrochemical deposition behavior of Li^+ on the lithium metal surface, enhances the stability of the electrode, and improves the electrochemical performance. In the process of optimizing the LMAs, we not only synergistically improve the deposition behavior of lithium from multiple aspects but also achieve the in-situ control of the SEI during the electrochemical cycling. This in-situ structural regulation strategy offers a novel approach to simultaneously address dendrite formation and interface design in lithium composite anodes.

Through a series of systematic experiments aimed at optimizing the elemental composition and concentration, we identified that 10wt% ZnF_2 is the optimal additive concentration. The resulting composite anode, denoted as LiF@LiZn10/Li, offers several advantages. Leveraging a LiF-rich interface and LiZn-strengthened bulk, the LiF@LiZn10/Li foil enables the fabrication of composite anodes with thicknesses ranging from 5 to 50 μm via roll-to-roll pressing. Additionally, it exhibits superior air resistance, enduring 144 hours in a 20% relative humidity environment. Furthermore, it effectively modifies the deposition behavior, leading to long-term cycling stability, surpassing 1300 hours in symmetrical cells under 1 mA cm^{-2} and 1 mA h cm^{-2}. The $LiFePO_4$||LiF@LiZn10/Li cell exhibited approximately triple the cycling life compared to cells with LMBs. A pouch cell featuring an NCM811 cathode and LiF@LiZn10/Li composite anode achieves excellent electrochemical performance with a specific energy of 350 Wh kg^{-1}.

Experimental

Material Preparation

Different metal fluorides such as ZnF_2 (Aladdin, 99%), MgF_2 (Aladdin, 98%), SnF_2 (Aladdin, 99%), and SbF_3 (Tansoole, 99%) were mixed with lithium metal to form different composite foil materials. The preparation process of the composite negative electrode material is shown in Figure 1a. First, high-purity lithium metal (China Energy Lithium Industry Co., Ltd.) was mixed with different metal fluorides through static pressing. Then, the mixtures were placed in a stainless steel container and heated to 250 °C in a glove box while maintaining the H_2O and O_2 content at less than 0.01 ppm. Continuous stirring was employed to ensure thorough mixing and reaction, resulting in the formation of homogeneous composite anode materials. After cooling to room temperature, the resulting composite materials were repeatedly rolled to prepare the LiF@LiM/Li foils in a dry chamber with a relative humidity (RH) of 5%.

In the symmetrical cells, we utilized LiF@LiM/Li electrodes and bare lithium electrodes with a diameter of 6 mm and a thickness of 200 μm. In full cells, circular pieces with a diameter of 12 mm were used for both the cathodes and anodes. The cathodes consisted of $LiFePO_4$ cathodes (China Shoto Ltd.) with a loading of 3.3 mA h cm^{-2} (20.6 mg cm^{-2}). The cathodes consisted of NCM811 cathodes (Caned) with a loading of 2.8 mA h cm^{-2} (15 mg cm^{-2}). The anode included 50 μm-thick LiF@LiZn10/Li foil anodes and 50 μm-thick bare-Li anodes. In the pouch cell, the NCM811 cathode had a size of 5*5 cm^2, and 40 μm-thick LiF@LiZn/Li foil anodes were employed.

Electrochemical Measurements

The electrochemical performance was measured by a Neware battery test system (CT-4008, Neware) at a temperature of 298K.

For symmetric cells, the current density was set at 1 mA cm^{-2} or 3 mA cm^{-2}, with an areal capacity of 1 mA h cm^{-2} or 3 mA h cm^{-2} in an ether electrolyte (1M LiTFSI DME:DOL = 1:1 with 2% $LiNO_3$) and a carbonate ester electrolyte (1M $LiPF_6$ in DMC:EC=7:3 with 2% VC).

For full cells, the current density was maintained at 0.5C in coin cells and 0.1C in the pouch cells. The cells were operated using a carbonate ester electrolyte. The potential range was 2.5-3.7 V for $LiFePO_4$ and 2.8-4.3 V for NCM811.

View Article Online
DOI: 10.1039/D4TA02434A

Electrochemical impedance spectroscopy (EIS) and linear sweep voltammetry (LSV) were performed using a Gamry. Nyquist plots of symmetric cells were obtained by EIS testing in the frequency range of 1 MHz to 0.1 Hz. Tafel plots for symmetrical cells were acquired by LSV testing in the voltage range of -0.2 V to 0.2 V at a scanning rate of 1 mV s^{-1}.

Characterization

X-ray diffraction (XRD) measurement was performed using a Bruker D8-Advance power X-ray diffractometer with Cu Kα radiation (λ = 0.15405 nm). X-ray photoelectron spectroscopy (XPS) analysis was performed on an American Thermo Fisher Scientific ESCALAB 250 Xi. To examine the morphology and structure of the samples, scanning electron microscopy (SEM) images and energy-dispersive X-ray spectrometry (EDS) mappings were performed by field emission scanning electron microscopy (SEM, FEI Quanta 250FEG) under an accelerated voltage of 5 kV. Tensile strength measurements were carried out in a dry chamber with a relative humidity (RH) of 5%.

Results and discussion

The symmetric cells were firstly fabricated to assess the cycling performance of prepared LiF@LiM/Li composites, the results were compared in Figure 1b. Under cycling conditions of 5 mA cm^{-2} and 5 mA h cm^{-2}, the cycle life of LiF@LiM/Li composite electrodes demonstrates remarkable improvements compared to the bare Li electrodes, which typically survive for approximately 70 hours. Specifically, the cycle life for LiF@LiSn/Li extends to 125 hours, LiF@LiSb/Li to 150 hours, LiF@LiMg/Li to 150 hours, and LiF@LiZn/Li significantly outperforms the others, lasting for 270 hours. The incorporation of MF$_n$ particles significantly enhances the cycling stability of the Li anode. Meanwhile, this indicates that the LiF@LiZn/Li foil can regulate the deposition behavior during the cycling process and exhibit longer cycle life. Furthermore, as illustrated in Figure 1c, owing to the modified Li/electrolyte interface through LiM alloys and LiF particles, the interface impedances of LiF@LiM/Li electrodes are notably reduced, with the most substantial reduction observed in the case of LiF@LiZn/Li electrode. This indicates that the LiF@LiZn/Li foil has better Li$^+$ transport ability, can form a high-performance SEI film during the cycling process, and reduces the internal impedance of the cell. Based on these electrochemical properties, ZnF$_2$ was selected as the primary material for optimizing lithium metal electrodes. Moreover, the cost-effectiveness of zinc also renders it a promising material for future industrial applications.

Further, to explore the influence of different ZnF$_2$ addition on electrochemical performance, the cycling performance of LiF@LiZn/Li electrodes with varying addition of ZnF$_2$ (samples denote as LiF@LiZn5/Li, LiF@LiZn10/Li, LiF@LiZn15/Li, LiF@LiZn33/Li; numbers represent the mass ratio of ZnF$_2$) was investigated. As Figure 1d presents, the LiF@LiZn5/Li exhibits a similar cycling performance to that of Li metal, suggesting the limited regulation effect through LiZn alloys and LiF particles results from the 5wt% ZnF$_2$ addition. Notably, LiF@LiZn10/Li, with a moderate ZnF$_2$ addition, demonstrates the longest cycle life of 270 hours. However, with further increases in ZnF$_2$ addition, the cycling life of LiF@LiZn15/Li and LiF@LiZn33/Li was reduced to 150 hours and 80 hours, respectively. The interface impedance results exhibit a similar trend with cycling performance in Figure 1e, following the order: Li> LiF@LiZn5/Li> LiF@LiZn15/Li> LiF@LiZn33/Li> LiF@LiZn10/Li. The

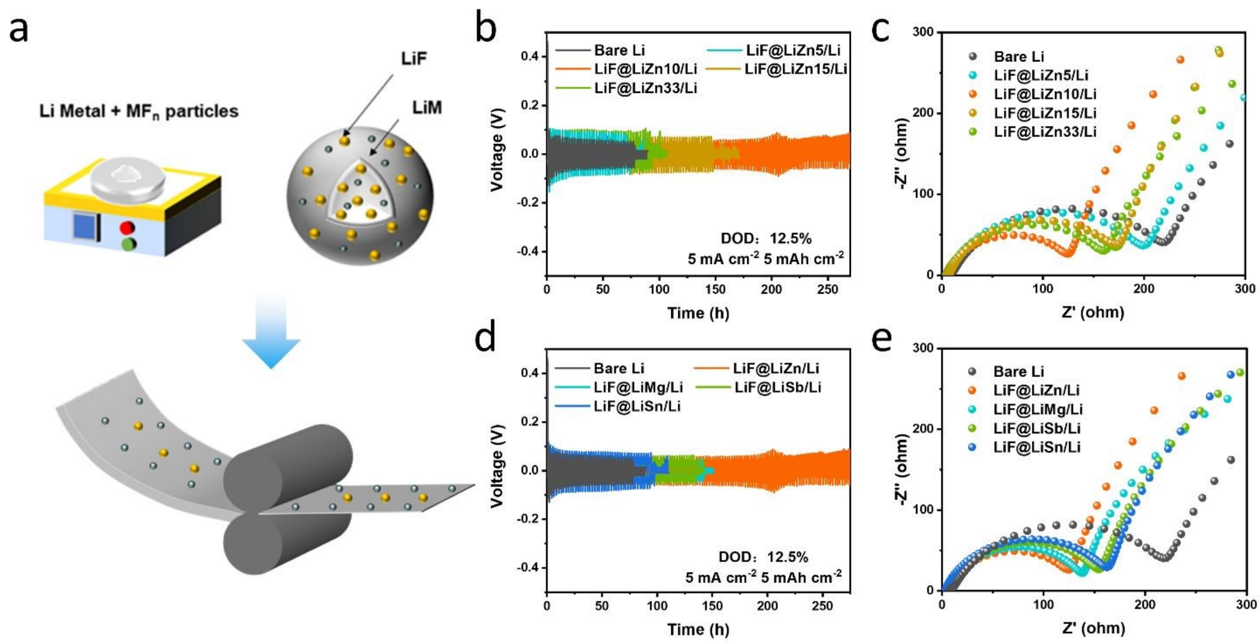

Figure 1. (a) Process diagram of the LiF@LiM/Li foils. (b) Cycle performance of bare Li and the LiF@LiM/Li (M = Zn, Mg, Sb, and Sn) symmetric cells at 5 mA cm^{-2} and 5 mA h cm^{-2}. (c) Nyquist plots of the LiF@LiM/Li (M = Zn, Mg, Sb, and Sn) foil electrodes in symmetric cells. (d) Cycle performance of bare Li and the LiF@LiZn/Li symmetric cells with different mass ratios (5%, 10%, 15%, 33%) at 5 mA cm^{-2} and 5 mA h cm^{-2}. (e) Nyquist plots of the LiF@LiZn/Li symmetric cells with different mass ratios (5%, 10%, 15%, 33%).

View Article Online
DOI: 10.1039/D4TA02431A

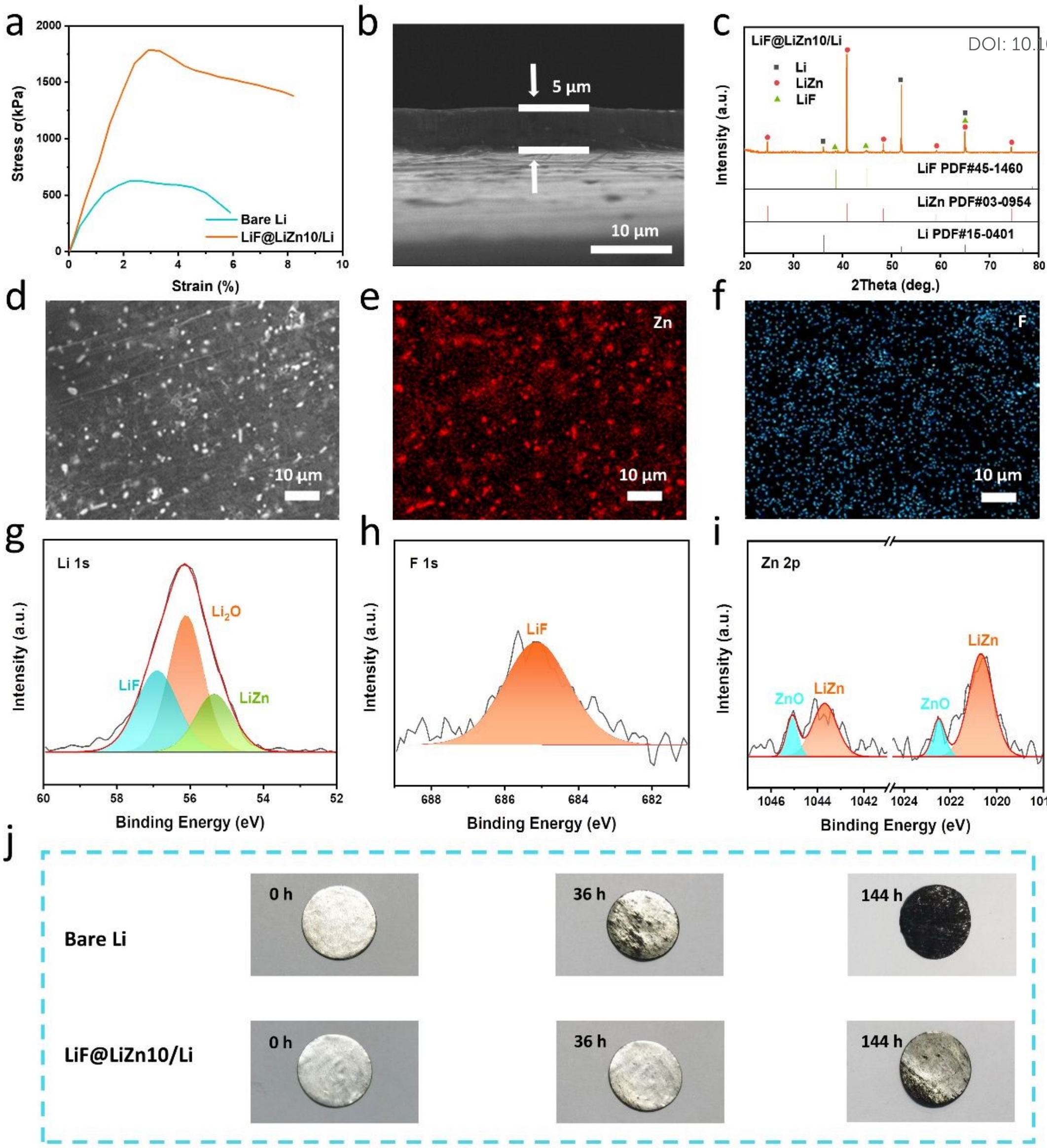

Figure 2. (a) Tensile stress deformation curves of bare Li and the LiF@LiZn10/Li foil. (b) SEM images of the LiF@LiZn10/Li foils with 5 μm. (c) XRD patterns of the LiF@LiZn10/Li foil. (d, e, f) SEM and EDS images displaying the distribution of the Zn element and F element on the surface of the LiF@LiZn10/Li foil. (g, h, i) High-resolution XPS spectra of the Li 1s, F1s, and Zn 2p of the LiF@LiZn10/Li foil. (j) The surfaces of bare Li electrode and the LiF@LiZn10/Li electrode exposed in a controlled environment with a relative humidity (RH) of 20%.

LiF@LiZn10/Li, with exceptional cycling stability and minimal impedance, was selected for further in-depth investigation.

It's well-recognized that the machinability of pure lithium metal is notorious. The mechanical strength of lithium is poor, which causes it to crack during rolling, especially when its thickness decreases down to 50 μm. Meanwhile, lithium can react with Cr_2O_3 on the roller surface, making it sticky to the stainless steel roller, and thus, the thinning of Li is troublesome, as shown in Figure S1.[32] Fortunately, the formation of LiZn alloys and LiF can dramatically change the mechanical properties of Li metal. As illustrated in Figure 2a, the LiF@LiZn10/Li foil exhibited a substantially improved tensile strength of approximately 1750 kPa, which is roughly three times that of the bare Li foil of approximately 650 kPa. The elongation at the break of LiF@LiZn10/Li (8%) is also higher than that of pure Li metal (4.5%). When the LiZn alloys and LiF particles are uniformly dispersed in the lithium matrix as finely distributed particles, they interact with dislocations, impeding their movement and increasing the deformation resistance of the alloys. Moreover, the dispersion of LiF particles and LiZn alloys on the surface of the LiF@LiZn10/Li foil acts as a contact inhibitor, which reduces the bonding between the roller and the LiF@LiZn10/Li foil. Benefiting from the enhanced mechanical strength and lowered stickiness, the prepared LiF@LiZn10/Li can be fabricated into the large-area foil with ultrathin thicknesses (from 50 μm to 5 μm, as displayed in Figures S2, S3) by a handily rolling procedure. The cross-section SEM images in Figures 2b, S4 imply that the 5 μm-thick and 50 μm-thick LiF@LiZn10/Li foil demonstrates a dense structure without holes in the matrix. Additionally, the thinned LiF@LiZn10/Li foil still maintains enough strength. As reported in Figure S5, the ultrathin LiF@LiZn10/Li foil can tolerate reiterative crimp, bending and stretching operation, without any cracks or tape

View Article Online
DOI: 10.1039/D4TA02431A

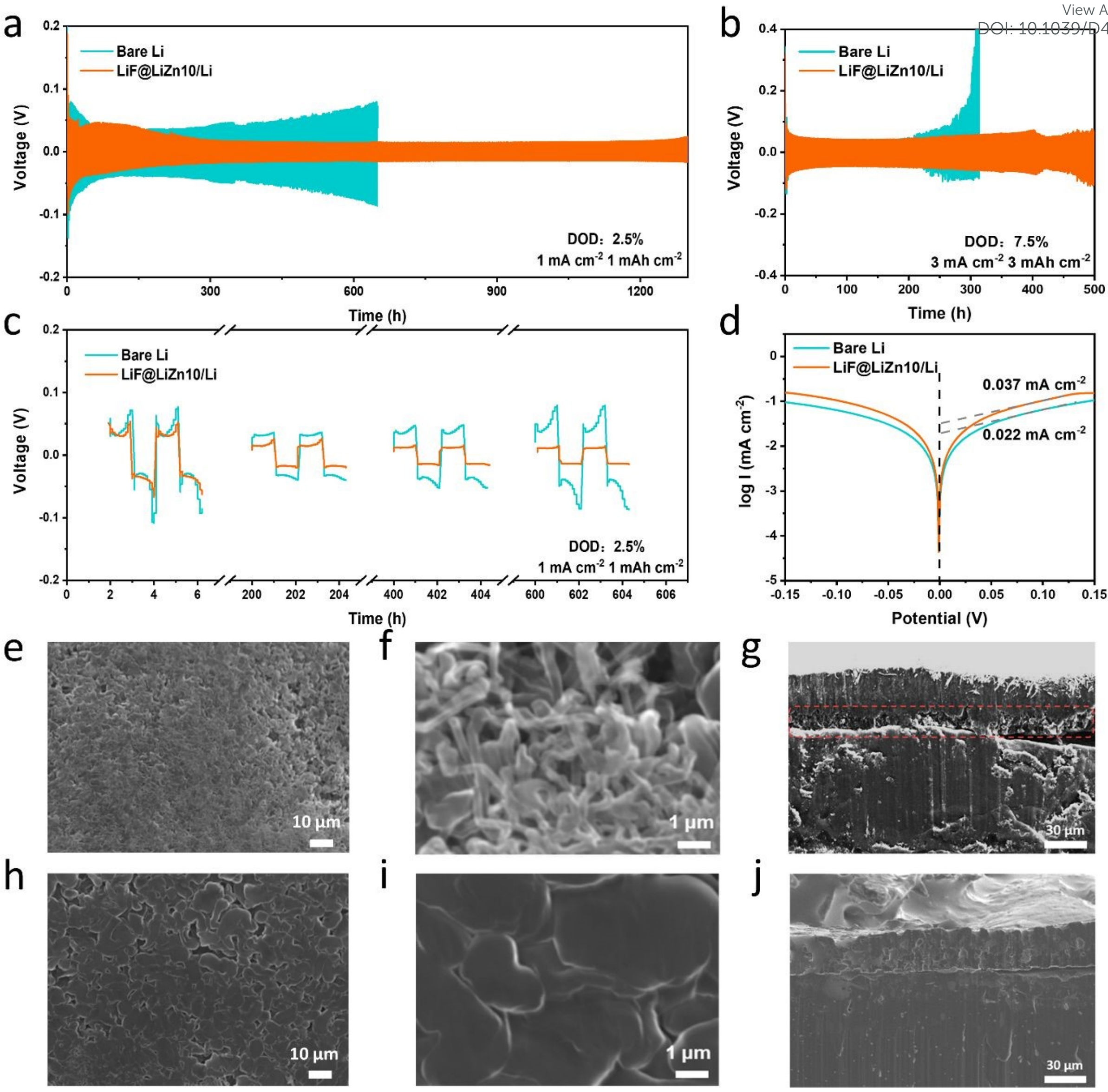

Figure 3. (a, c) Cyclic performance of bare Li and the LiF@LiZn10/Li symmetric cells at 1 mA cm^{-2} and 1 mA h cm^{-2}. (b) Cyclic performance of bare Li and the LiF@LiZn10/Li symmetric cells at 3 mA cm^{-2} and 3 mA h cm^{-2}. (d) The Tafel plots of bare Li and the LiF@LiZn10/Li symmetric cells. (e, f, g) SEM images of the morphology after Li plating on bare Li electrode with 6 mA h cm^{-2}. (h, i, j) SEM images of the morphology after Li plating on the LiF@LiZn10/Li electrode with 6 mA h cm^{-2}.

break, which facilitates the electrode fabrication process in practical application. The controlled thickness of the LiF@LiZn10/Li foil supports the construction of high-energy density Li metal batteries with a limited N/P ratio.

The XRD was performed to explore the phase composition of LiF@LiZn10/Li foil. The results are shown in Figure 2c. The peaks corresponding to the intermetallic LiZn alloys are significantly observed at 24.71°, 40.99°, and 65.19°. The peaks of LiF, appearing at 38.7°, 44.99°, and 65.49°, demonstrate weaker intensity. The EDS mapping in Figures 2d-f suggests that these particles are LiZn alloys and LiF particles, which are uniformly dispersed on the surface of the LiF@LiZn10/Li. The cross-section image in Figure S6 further indicates that the formed LiZn and LiF are throughout the whole matrix. Furthermore, the distribution of LiZn alloys and LiF particles in the matrix also appears to be relatively uniform.

The surface composition was further investigated by XPS analysis in Figure 2g-i. The Li 1s peak appeared at 56.9 eV and the F 1s peak observed at 685.0 eV is attributed to LiF. The Li 1s peak was observed at 55.3 eV, the Zn 2p doublet peaks were observed at 1043.6 eV and 1020.6 eV, indicating the presence of LiZn alloys on the foil. Additionally, due to surface oxidation, peaks arising from ZnO and Li_2O in the Li 1s and Zn 2p spectra can be detected.

While the oxidation layer of the Li metal surface is composed of fragile Li_2O, LiOH which is unable to resist corrosion of H_2O and O_2, the ZnO and LiF components on the LiF@LiZn10/Li can protect underlying Li from continuous oxidation.[38-40] As a result, the air stability of the LiF@LiZn10/Li gets a significant improvement. Figure 2j records the visual change of pure Li and the LiF@LiZn10/Li during the exposure to the 20 RH% atmosphere. It's obvious that the pure Li is corroded severely and after 140-h exposure, the surface of Li

View Article Online
DOI: 10.1039/D4TA02431A

demonstrates a dark black, indicating complete oxidation of the surface. However, with the protection of surficial ZnO and LiF, the LiF@LiZn10/Li/Li retained the metallic luster after 36-h exposure. Even after 140-h exposure, the surface oxidation was weak and the foil appeared grayish. Meanwhile, both electrodes were also tested in a dry chamber with a 10% relative humidity in Figure S7 and the same results can be obtained. The improved air stability of the LiF@LiZn10/Li would reduce the moisture control requirement for the manufacturing of LMBs, which could lower the cost of LMBs assembly.

The LiF@LiZn10/Li electrode exhibits a practical capacity of about 10.37 mA h (Figure S8). Meanwhile, the specific capacity of the LiF@LiZn10/Li electrode has slightly decreased, measuring around 3263 mA h g^{-1} (Figure S8). Excluding the influence of surface oxidation, the test results were in good agreement with the theoretical calculations in Figure S9 and Table S1.

Symmetrical cells were constructed to assess the electrochemical performance of the LiF@LiZn10/Li foil electrode utilizing in ether electrolyte. The thickness of the LiF@LiZn10/Li foil was maintained at approximately 50 μm. As depicted in Figure 3a, the LiF@LiZn10/Li ||LiF@LiZn10/Li cell exhibited a cycling duration of approximate 1300 hours under conditions of 1 mA cm^{-2} and 1 mA h cm^{-2}. In contrast, the Li||Li cell could only cycle for 700 hours. When the current density was increased to 3 mA cm^{-2} and the capacity reached 3 mA h cm^{-2} as shown in Figure 3b, both the LiF@LiZn10/Li and the bare Li electrodes experienced a substantial decrease in cycle life, consistent with the phenomenon of rapid lithium dendrite growth at high current densities. However, the LiF@LiZn10/Li exhibited a cycle life of approximately 500 hours, whereas the bare Li electrode could only endure for 260 hours. Under testing conditions with 20% or even 40% depth of discharge (DOD) in Figure S10, the LiF@LiZn10/Li symmetric cells demonstrate good cycling performance. The presence of the lithiophilic element Zn contributed to a significantly lower polarization overpotential of the LiF@LiZn10/Li electrode compared to the bare Li electrode, as illustrated in Figure 3c. Moreover, due to the stable interface between the LiF@LiZn10/Li and the electrolyte, the polarization voltage of the LiF@LiZn10/Li foil electrodes tended to stabilize as cycling progressed. Conversely, the SEI on the Li anode's surface was continuously destroyed and reconstructed, resulting in a continuous increase in polarization overpotential. Furthermore, the performance of the bare Li electrode and the LiF@LiZn10/Li foil electrode was evaluated using a commercial carbonate ester electrolyte. The LiF@LiZn10/Li foil electrode demonstrated more stable electrochemical cycling than the bare Li electrodes (Figure S11), concurrently exhibiting lower deposition potential.

The lower polarization and longer stable cycling life of the LiF@LiZn10/Li foil can be supported by the higher exchange current density. The exchange current density of the LiF@LiZn10/Li foil electrode was determined through Tafel testing. As depicted in Figure 3d, the exchange current density of the LiF@LiZn10/Li foil electrode was measured at 0.037 mA cm^{-2}, which was higher than the 0.022 mA cm^{-2} observed for the bare Li electrode. This indicates that the LiF@LiZn10/Li foil electrode exhibited considerably faster charge transfer and improved electrochemical reaction kinetics. To validate the significant impact of the LiF@LiZn10/Li foil in enhancing the reaction kinetics of the electrode, EIS tests were conducted on both the LiF@LiZn10/Li||LiF@LiZn10/Li cell and the Li||Li cell. The charge transfer resistance (R_{ct}) and solid electrolyte interphase resistance (R_{SEI}) of the LiF@LiZn10/Li||LiF@LiZn10/Li cell exhibit a gradual reduction during cycling, which aligns with the observed decrease in polarization as shown in Figure S12a. Furthermore, after 100 cycles of 1 mA cm^{-2} and 1 mA h cm^{-2}, the symmetrical cell with the LiF@LiZn10/Li electrode demonstrates lower R_{ct} and R_{SEI} compared to the Li||Li cell (Figure S12b). This reduction can be attributed to the presence of LiZn alloys and LiF particles in the LiF@LiZn10/Li foil electrode, which contributes to the improvement in reaction kinetics.

The excellent electrochemical performance of the LiF@LiZn10/Li foil is attributed to significantly improved Li deposition behavior on its surface. The surface morphology of the bare Li and the LiF@LiZn10/Li foil after Li deposition of 6 mA h cm^{-2} at 1 mA cm^{-2} was characterized using SEM. As displayed in Figures 3e and 3f, the surface of bare Li after Li deposition demonstrates a porous and loosely arranged structure. Upon closer examination, it is evident that Li deposition predominantly manifests in dendritic forms. These dendrites exhibit a high aspect ratio, with lengths exceeding 5 μm and diameters of approximately 100 nm. In contrast, the LiF@LiZn10/Li surface after deposition displays lower porosity, resulting in a smoother and denser surface in Figures 3h and 3i. Figure 3i reveals that the Li deposition is uniformly distributed and primarily in the form of blocks and rods. As shown in Figure 3g, the thickness of the Li deposition reaches approximately 44-48 μm. During Li deposition on the lithium metal surface, voids appear, causing the volume expansion of the deposition layer. In contrast, Figure 3j shows that the deposited Li on the LiF@LiZn10/Li surface is more uniform and dense, and the thickness of the deposition layer is noticeably reduced and similar to the theoretical thickness of approximately 33 μm. These observations indicate that the LiF@LiZn10/Li electrode enables homogeneous Li diffusion, promotes uniform Li deposition, and effectively suppresses the formation of Li dendrites.

The improved Li deposition behavior can be attributed to the presence of LiZn alloys and LiF particles on the surface of the LiF@LiZn10/Li foil electrode. The heterogeneous lithium nucleation is the source of the formation of lithium dendrites. The nature-formed fragile SEI fails to effectively restrain the growth of these dendrites. Nevertheless, the LiZn alloys present on the surface of the LiF@LiZn10/Li foil effectively offer uniform nucleation sites, reducing the nucleation overpotential of Li deposition and promoting the even deposition of Li^+ during the whole cycle life. Concurrently, compared to Figure 4a and Figure 4d, the content of LiF increased significantly in the SEI of the LiF@LiZn10/Li foil electrode after five cycles through XPS analysis. It was due to a surface of the LiF@LiZn10/Li foil with LiF-rich particles. The LiF component facilitates the formation of a SEI rich in LiF during the deposition process. This LiF-rich SEI alters the distribution of Li flux at the interface, leading to the formation of short and wide Li deposition morphologies instead of slender and elongated dendritic structures. Additionally, we speculate that the in-situ regulation of LiF in the formation of the SEI on the lithium anode is a continuous process throughout the electrochemical cycling life.

To verify the working mechanism of LiF in the LiF@LiZn10/Li foil electrode during the cycling, the Li||Li and Li||LiF@LiZn10/Li cells

View Article Online
DOI: 10.1039/D4TA02431A

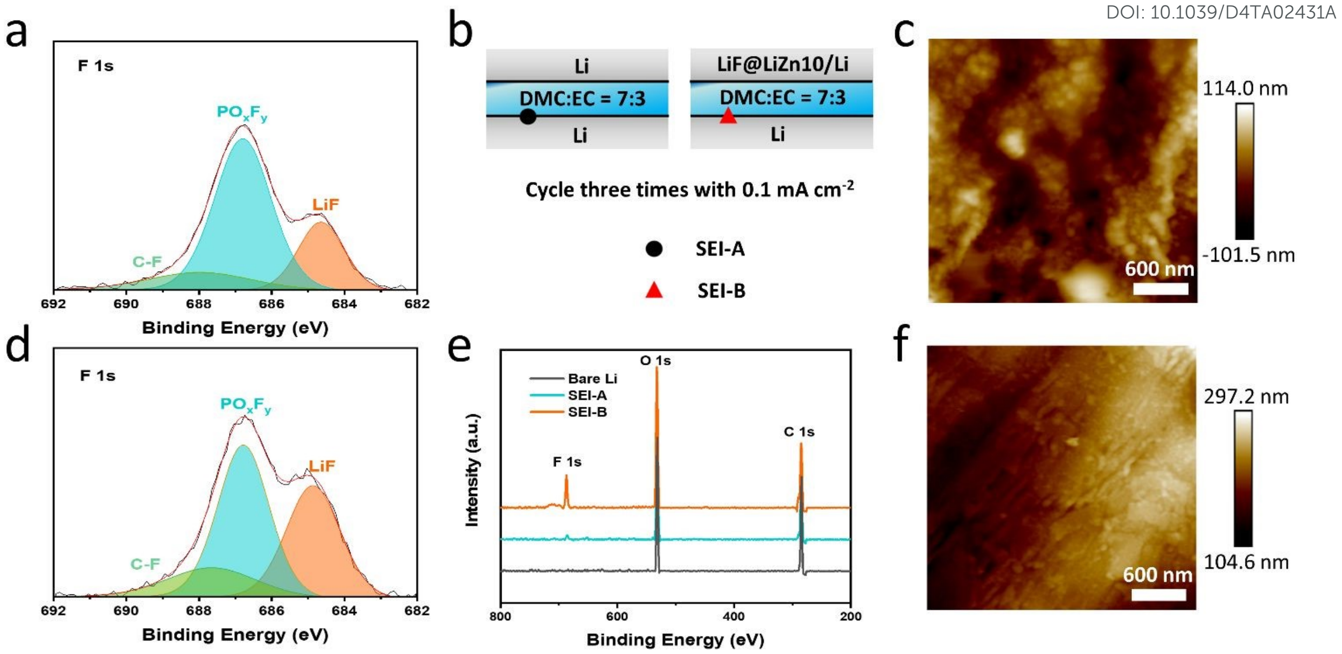

Figure 4. (a) High-resolution XPS spectra of F 1s on electrode surface of bare Li symmetric cells after 5 cycles. (b) Illustrations of the Li||Li symmetric cell (left) and the Li||LiF@LiZn10/Li symmetric cell (right). (c) AFM image of the SEI morphology on bare Li surface. (d) High-resolution XPS spectra of F 1s on electrode surface of the LiF@LiZn10/Li symmetric cells after 5 cycles. (e) XPS survey spectra obtained at bare Li, SEI-A, and SEI-B. (f) AFM images of the SEI morphology on the LiF@LiZn10/Li surface.

with DME:EC (without $LiPF_6$) were assembled, as indicated in Figure 4b. The XPS was performed to obtain the surface composition of the Li electrode in Li||Li cell (SEI-A) and Li||LiF@LiZn10/Li (SEI-B) after three cycles at 0.1 mA cm^{-2}. The surface of Li foil without electrolyte immersing and cycling was also analyzed for comparison. Survey XPS spectra showed the presence of F, O, and C signals at the SEI-A, and SEI-B in Figure 4e. The intensity of the F 1s signals at SEI-B was significantly stronger than that at SEI-A and bare Li. Subsequently, a semi-quantitative analysis of the elemental contents of F and O at different locations was conducted (Figure S14). The F content at SEI-B was nearly five times higher than that at SEI-A, while the O content at SEI-B was comparable to that at SEI-A. Considering that the electrolyte is free of the F element, the increased intensity of the F 1s signals at SEI-B arises from the counter of the LiF@LiZn10/Li foil electrode. Specifically, the LiF in the LiF@LiZn10/Li electrode dissolved in the solvent electrolyte during cycling, and participated in the formation of the SEI layer on the counter electrode (Li). As a result, a rich LiF-based SEI film was formed on the bare Li electrode in the Li||LiF@LiZn10/Li cell. It is worth mentioning that the F content of SEI-A is slightly higher than that of the bare Li electrode, suggesting that the F element was enriched on the electrode surface after cycling. Therefore, it can be concluded that LiF from the LiF@LiZn10/Li foil electrode can dissolve into the electrolyte, redistribute locally on the anode surface, and participate in the formation of the SEI, forming a LiF-rich interphase layer during the cycling.[41] During cycling, the content of LiF in the SEI continuously increases (Figure S15). The deposition and dissolution of Li^+ and lithium metal in the LiF@LiZn10/Li electrode continuously expose LiF particles in the matrix to the electrolyte. Simultaneously, the dissolution mechanism of LiF particles ensures a continuous supply of LiF particles into the electrolyte, and with the Li deposition, it participates in the formation of the SEI. This process enables the formation of an SEI rich in LiF during cycling. After three cycles at 1 mA cm^{-2} and 1 mA h cm^{-2}, the AFM images of the electrode surface are shown in Figures 4c and 4f. Figure 4c illustrates a rough SEI film on the surface of bare lithium, characterized by numerous pits and an uneven surface. In contrast, Figure 4f demonstrates that the SEI film formed on the LiF@LiZn10/Li electrode exhibits a remarkably smooth and uniform surface with low roughness. Furthermore, we evaluated the mechanical properties of the SEI using the Derjaguin-Müller-Toporov (DMT) modulus. The SEI formed on the LiF@LiZn10/Li surface exhibits a higher average DMT modulus of 4.08 GPa, compared to 2.53 GPa for the SEI on the bare Li surface. The AFM results suggest that the LiF@LiZn10/Li electrode improves the Li deposition morphology, enhances the mechanical strength of the SEI, and optimizes its physicochemical properties during cycling. The LiF-rich SEI effectively enhances Li^+ interface transport, suppresses lithium dendrite growth, and promotes a more uniform and stable electrochemical behavior of Li^+ on the surface of the lithium metal anode.[42] Additionally, the incorporation of LiF improves the stability of the SEI, effectively reducing the consumption of lithium metal, mitigating electrolyte consumption, and significantly enhancing the overall stability and cycle life of the cells.[43, 44]

To evaluate the potential application of the LiF@LiZn10/Li foil electrode in full cells, commercial $LiFePO_4$ cathodes (3.3 mA h cm^{-2}) were used to couple with the as-prepared LiF@LiZn10/Li composite electrodes (50 µm). As illustrated in Figure 5a, the $LiFePO_4$

View Article Online
DOI: 10.1039/D4TA02431A

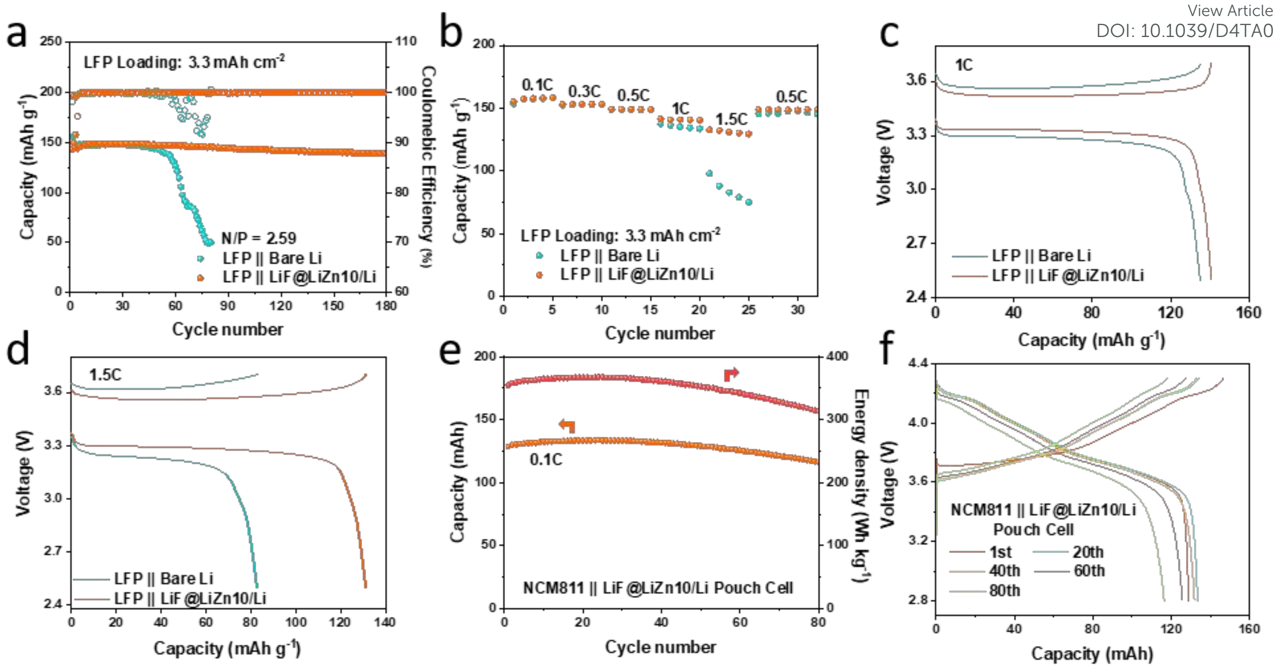

Figure 5. (a) Cycling performance of LiFePO$_4$||bare Li and LiFePO$_4$||LiF@LiZn10/Li full cells at 0.5C. (b) The rate capability of LiFePO$_4$||bare Li and LiFePO$_4$||LiF@LiZn10/Li full cells. (c, d) The Corresponding voltage profiles of LiFePO$_4$||bare Li and LiFePO$_4$||LiF@LiZn10/Li full cells at 1C and 1.5C. (f) Cycling performance of the NCM811||LiF@LiZn10/Li pouch cell. (g) The Corresponding voltage profiles of the NCM811||LiF@LiZn10/Li pouch cell at different cycles.

||LiF@LiZn10/Li cell with a practical N/P ratio of 2.59 exhibits superior cycling performance over 180 cycles, maintaining a steady CE of over 98% at 0.5C. In contrast, the LiFePO$_4$||bare-Li cell exhibits rapid capacity decay after 50 cycles, accompanied by lower and fluctuated CE in Figure 5a. Moreover, by pairing with an ultrathin LiF@LiZn10/Li composite electrode (20 µm), a full cell with a practical N/P ratio of 1.04 was further constructed and investigated. Despite the limited amount of Li, the cell still offers stable cycling over 30 cycles with a capacity retention of 94% at 0.5 C in Figure S16.

Figure 5b illustrates that the LiFePO$_4$||LiF@LiZn10/Li full cell exhibits superior rate performance, particularly at high current rates. Notably, the LiFePO$_4$||LiF@LiZn10/Li full cell demonstrates reversible capacities of 140.8 mA h g^{-1} at 1C and 131.2 mA h g^{-1} at 1.5C, surpassing the capacities of 135.1 mA h g^{-1} and 82.8 mA h g^{-1} at 1C and 1.5C, respectively, for the LiFePO$_4$||bare Li cell (Figure 5c, 5d). Its CE is included in Figure S17. This enhanced rate performance can be attributed to the rapid transfer of Li$^+$ ions at the interfaces and improved Li plating and stripping kinetics, leading to a reduction in the polarization potential during the electrochemical cycling of the LiF@LiZn10/Li electrode.

Furthermore, a pouch cell was constructed to assess the practical application potential of the LiF@LiZn10/Li electrode (Figure S18). As depicted in Figure S18, the pouch cell utilized NCM811 as the positive electrode material, a 40 µm-thick LiF@LiZn10/Li foil as the negative electrode, and a 3.18 g Ah^{-1} injection ratio (Table S2). The initial discharge capacity of the cell reached 130.2 mA h at 0.1C, corresponding to a high energy density of 350 Wh kg^{-1}. The pouch cell exhibited excellent cycling performance, maintaining over 80% of its capacity after 80 cycles at 0.1C (Figures 5e and 5f), accompanied by a CE of over 99.1% during the initial 50 cycles (Figure S19). This can be attributed to the formation of a LiF-rich SEI and the uniform deposition of lithium on the surface of the LiF@LiZn10/Li foil electrode during cycling. Additionally, SEM images of the LiF@LiZn10/Li electrode after cell cycling revealed smooth and dense Li deposition on the surface (Figures S20a and S20b). It is worth mentioning that the carbonate ester electrolyte ensures stable cycling of the pouch cell below 4.3 V (Figure S21). These results indicate that the LiF@LiZn10/Li foil exhibits exceptional electrochemical performance, offering valuable insights for the utilization of lithium metal in batteries with high energy density and long cycle life.

Conclusions

In conclusion, we propose the LiF@LiZn10/Li foil electrode with an ultrathin lithium. This anode material is formed by the in-situ formation of LiZn alloys and LiF nanoparticles composite with lithium metal. Homogeneously dispersed LiZn alloys and LiF particles contribute to secondary strengthening, thereby significantly improving the mechanical properties and stability in ambient air of anode materials. The LiF@LiZn10/Li foil can be prepared with a thickness of 5-50 µm lithium foil. Furthermore, the LiZn alloys and LiF particles embedded in the electrode enhance Li$^+$ diffusion kinetics. During the whole electrochemical cycling life, the presence of the LiZn alloys provides uniform nucleation sites for Li deposition, and LiF particles dissolve into the electrolyte and participate in the formation of SEI, which enhances the cyclic stability of the electrode and improves the cycling performance of the batteries. The results show that the LiF@LiZn10/Li foil electrode exhibits long-term and stable cycle stability in symmetrical cells and full cells. In addition, the high energy density (350 Wh kg^{-1}) prepared by the LiF@LiZn10/Li foil

View Article Online
DOI: 10.1039/D4TA02431A

electrode shows good cycling performance. Finally, this work proposes an in-situ structural regulation strategy that addresses the non-uniform nucleation and interface design of lithium composite anodes, providing a pathway for the development of ultra-thin Li metal anodes to achieve high energy density and long cycle life in batteries.

Author Contributions

Jing Tao: Investigation, Methodology, Formal Analysis, Writing-original draft. Can Zhang: Writing-review & editing, Software. Xueyang Li: Writing-review & editing, Methodology. Xinlong Chen: Investigation, Formal Analysis. Chenzhen Ji: Resources, Funding acquisition. Wang Wan: Resources, Supervision, Project administration. Chao Wang: Writing-review & editing, Methodology, Supervision.

Conflicts of interest

There are no conflicts to declare.

Acknowledgements

This work was supported by the National Key Research and Development Program of China (2022YFB3803400), the Shanghai Pujiang Program (22PJ1413400), and the Fundamental Research Funds for Central Universities. The authors gratefully acknowledge the financial support from National Engineering Research Center of New Energy Vehicles, and Power Systems and Shanghai Key Lab of Vehicle Aerodynamics and Vehicle Thermal Management Systems.

Notes and references

1. B. Liu, J.-G. Zhang and W. Xu, *Joule*, 2018, **2**, 833-845.
2. W. Xu, J. Wang, F. Ding, X. Chen, E. Nasybulin, Y. Zhang and J.-G. Zhang, *Energy Environ. Sci.*, 2014, **7**, 513-537.
3. P. Bai, J. Li, F. R. Brushett and M. Z. Bazant, *Energy Environ. Sci.*, 2016, **9**, 3221-3229.
4. H. Zhang, Y. Yang, D. Ren, L. Wang and X. He, *Energy Stor. Mater.*, 2020, **36**.
5. C. Luo, H. Hu, T. Zhang, S. Wen, R. Wang, Y. An, S.-S. Chi, J. Wang, C. Wang, J. Chang, Z. Zheng and Y. Deng, *Advanced Materials*, 2022, **34**, 2205677, 147-170.
6. S. S. Zhang, *ACS Appl. Energy Mater.*, 2018, **1**, 910-920.
7. X. Xu, S. Wang, H. Wang, C. Hu, Y. Jin, J. Liu and H. Yan, *J. Energy Chem.*, 2018, **27**, 513-527.
8. C. Jin, T. Liu, O. Sheng, M. Li, T. Liu, Y. Yuan, J. Nai, Z. Ju, W. Zhang, Y. Liu, Y. Wang, Z. Lin, J. Lu and X. Tao, *Nat. Energy*, 2021, **6**, 378-387.
9. K.-H. Chen, K. N. Wood, E. Kazyak, W. S. LePage, A. L. Davis, A. J. Sanchez and N. P. Dasgupta, *J. Mater. Chem. A*, 2017, **5**, 11671-11681.
10. C.-J. Huang, B. Thirumalraj, H.-C. Tao, K. N. Shitaw, H. Sutiono, T. T. Hagos, T. T. Beyene, L.-M. Kuo, C.-C. Wang, S.-H. Wu, W.-N. Su and B. J. Hwang, *Nature Commun.*, 2021, **12**, 1452.
11. S. J. Yang, F. N. Jiang, J. K. Hu, H. Yuan, X. B. Cheng, S. Kaskel, Q. Zhang and J. Q. Huang, *Electron.*, 2023, **1**, e8.
12. Z. Su, J. Zhang, J. Jin, S. Yang and G. Li, *Chem. Eng. J.*, 2022, **430**, 132865.
13. A. Jana, S. I. Woo, K. S. N. Vikrant and R. E. García, *Energy Environ. Sci.*, 2019, **12**, 3595-3607.
14. R. Zhang, X. Chen, X. Shen, X.-Q. Zhang, X.-R. Chen, X.-B. Cheng, C. Yan, C.-Z. Zhao and Q. Zhang, *Joule*, 2018, **2**, 764-777.
15. X. Wang, Y. He, S. Tu, L. Fu, Z. Chen, S. Liu, Z. Cai, L. Wang, X. He and Y. Sun, *Energy Stor. Mater.*, 2022, **49**, 135-143.
16. J.-F. Ding, Y.-T. Zhang, R. Xu, R. Zhang, Y. Xiao, S. Zhang, C.-X. Bi, C. Tang, R. Xiang, H. S. Park, Q. Zhang and J.-Q. Huang, *Green Energy Environ.*, 2023, **8**, 1509-1530.
17. Z. Zhang, Y. Jin, Y. Zhao, J. Xu, B. Sun, K. Liu, H. Lu, N. Lv, Z. Dang and H. Wu, *Nano Res.*, 2021, **14**, 3999-4005.
18. J. Cao, Y. Shi, A. Gao, G. Du, M. Dilxat, Y. Zhang, M. Cai, G. Qian, X. Lu, F. Xie, Y. Sun and X. Lu, *Nat. Commun.*, 2024, **15**, 1354.
19. S. Liu, J. Zhao, F. Li, Y. Zhao and G. Li, *J. Mater. Chem. A*, 2022, **10**, 5221-5229.
20. S. Han, Z. Li, Y. Zhang, D. Lei and C. Wang, *Energy Stor. Mater.*, 2022, **48**, 384-392.
21. C. Li, S. Tu, X. Ai, S. Gui, Z. Chen, W. Wang, X. Liu, Y. Tan, H. Yang and Y. Sun, *Energy Environ. Mater.,* 2023, **6**, e12267.
22. K. Yan, Z. Lu, H.-W. Lee, F. Xiong, P.-C. Hsu, Y. Li, J. Zhao, S. Chu and Y. Cui, *Nat. Energy*, 2016, **1**, 16010.
23. C. Sun, A. Lin, W. Li, J. Jin, Y. Sun, J. Yang and Z. Wen, *Adv. Energy Mater.*, 2020, **10**, 1902989.
24. Y. Cheng, R. Lu, K. Amin, B. Zhang, Q. Zhou, C. Li, L. Mao, Z. Zhang, X. Lu and Z. Wei, *ACS Appl. Energy Mater.*, 2021, **4**, 6106-6115.
25. E. Peled and S. Menkin, *J. Electrochem. Soc.*, 2017, **164**, A1703-A1719.
26. Y. Gu, E.-M. You, J.-D. Lin, J.-H. Wang, S.-H. Luo, R.-Y. Zhou, C.-J. Zhang, J.-L. Yao, H.-Y. Li, G. Li, W.-W. Wang, Y. Qiao, J.-W. Yan, D.-Y. Wu, G.-K. Liu, L. Zhang, J.-F. Li, R. Xu, Z.-Q. Tian, Y. Cui and B.-W. Mao, *Nat. Commun.*, 2023, **14**, 3536.
27. H. Wu, H. Jia, C. Wang, J. G. Zhang and W. Xu, *Adv. Energy Mater.*, 2020, **11**, 2003092.
28. Y. Li, W. Huang, Y. Li, A. Pei, D. T. Boyle and Y. Cui, *Joule*, 2018, **2**, 2167-2177.
29. Z. Li, Y. Chen, X. Yun, P. Gao, C. Zheng and P. Xiao, *Adv. Funct. Mater.*, 2023, **33**, 2300502.
30. Y. Guo, S. Pan, X. Yi, S. Chi, X. Yin, C. Geng, Q. Yin, Q. Zhan, Z. Zhao, F. M. Jin, H. Fang, Y. B. He, F. Kang, S. Wu and Q. H. Yang, *Adv. Mater.*, 2023, **36**, 2308493.
31. X. Y. Yue, Y. X. Yao, J. Zhang, S. Y. Yang, Z. Li, C. Yan and Q. Zhang, *Adv. Mater.*, 2022, **34**, 2110337.
32. W. Wu, W. Luo and Y. Huang, *Chem. Soc. Rev.*, 2023, **52**, 2553-2572.
33. A. Masias, N. Felten, R. Garcia-Mendez, J. Wolfenstine and J. Sakamoto, *J. Mater. Sci.*, 2019, **54**, 2585-2600.
34. C. Zhang, H. Fan, X. Chen, H. Xu, J. Lou, Y. Li, Y. Huang and S. Li, *Energy Environ. Sci.*, 2022, **15**, 5251-5260.
35. Z. Guo, T. Wang, D. Wang, H. Xu, X. Liu, Y. Dai, H. Yang, Y. Huang and W. Luo, *ACS Nano*, 2023, **17**, 14136-14143.
36. J. Gao, C. Chen, Q. Dong, J. Dai, Y. Yao, T. Li, A. Rundlett, R. Wang, C. Wang and L. Hu, *Adv. Mater.*, 2021, **33**, 2005305.
37. J. Zhang, X. Yue, Z. Wu, Y. Chen, Y. Bai, K. Sun, Z. Wang and Z. Liang, *Nano Lett.*, 2023, **23**, 9609-9617.
38. J. Wu, L. Yuan, Z. Li, X. Xie and Y. Huang, *Mater. Horiz.*, 2020, **7**, 2619-2634.
39. D. Lin, Y. Liu, W. Chen, G. Zhou, K. Liu, B. Dunn and Y. Cui, *Nano Lett.*, 2017, **17**, 3731-3737.

View Article Online
DOI: 10.1039/D4TA02431A

40. H. Li, F. Zhang, W. Wei, X. Zhao, H. Dong, C. Yan, H. Jiang, Y. Sang, H. Chen, H. Liu and S. Wang, *Adv. Energy Mater.*, 2023, **13**, 2301023.
41. G. Li, X. Duan, X. Liu, R. Zhan, X. Wang, J. Du, Z. Chen, Y. Li, Z. Cai, Y. Shen and Y. Sun, *Adv. Mater.*, 2022, **35**, 2207310.
42. A. Ramasubramanian, V. Yurkiv, T. Foroozan, M. Ragone, R. Shahbazian-Yassar and F. Mashayek, *J. Phys. Chem. C*, 2019, **123**, 10237-10245.
43. J. Tan, J. Matz, P. Dong, J. Shen and M. Ye, *Adv. Energy Mater.*, 2021, **11**, 2100046.
44. Q.-K. Zhang, X.-Q. Zhang, J. Wan, N. Yao, T.-L. Song, J. Xie, L.-P. Hou, M.-Y. Zhou, X. Chen, B.-Q. Li, R. Wen, H.-J. Peng, Q. Zhang and J.-Q. Huang, *Nat. Energy*, 2023, **8**, 725-735.